Chapter 9
Two-Dimensional Non-similar Flows

In the foregoing chapters, we had strictly been limited to the self-similar flows due to moving continuous surfaces of different geometries. Despite the devoted efforts spent in the previous part, it is yet a matter of reality that the class of self-similar solutions in all the considered cases is very restricted being strictly limited to the power-law and the exponential wall velocities. In particular applications, the situations, in general, need not to follow the power-law or exponential wall velocities only. In such circumstances, the wall velocity functions are free to adopt any differentiable from other than the power-law and the exponential forms. Such classes of velocity functions are really very large in comparison with the self-similar ones and have a great potential to cover almost all the other possible wall velocities occurring in technological applications. Corresponding to all other forms of the wall velocity functions, the flow will essentially be non-similar in nature. In view of the available literature on the boundary-layers due to moving continuous surfaces, no significant efforts have so far been spent in this direction. In this regard, the current part of this book is of great importance where we intend to introduce the non-similar flows due to moving continuous surfaces. In Chaps. 9 and 10, the spatial non-similarity in the planner two-dimensional and the axially symmetric cases has been considered, respectively, whereas the temporal non-similarity is considered in Chap. 11.

9.1 Non-similar Governing Equations

The previously considered governing system (5.2)–(5.4) for the two-dimensional self-similar flows is equally applicable to the case of non-similar flows considered in this section. Different from the self-similar flows, the variable wall velocity $u_w(x)$ neither does obey the power-law nor the exponential form in this case. Such a violation of the self-similarity criterion is actually responsible for the *non-similar* designation of the current viscous flows. With this breaking of the similarity

A. Mehmood, *Viscous Flows*, Mathematical Engineering,
DOI 10.1007/978-3-319-55432-7_9

criterion, the velocity function $u_w(x)$ is free to assume any other form falling out of the scope of similarity wall velocities. Such other forms are finally charged by a partial differential equation to be solved, instead of ordinary differential equation, for the non-similar flows.

Till the third quarter of the last century, the non-similar flows had been thought to be difficult to handle because of the limited availability of high-performance computing machines. This restriction has now been elevated completely because of the availability of cheap but high-performance computing machines as a consequence of the advent of modern technology. On the other hand, the tremendous developments in the CFD have now made the solution of non-similar equations equally that easy as does the solution of *odes*.

The non-similar formulation of the governing system (5.2)–(5.4) comes directly from the self-similar formulation with the consideration that $\frac{\partial f}{\partial x} \not\equiv 0$, whereas in the self-similar flows $\frac{\partial f}{\partial x} \equiv 0$. In this way, the similarity transformations (6.5) do also work in the non-similar case but with the modified form of the stream function ψ, given by

$$\psi = \sqrt{u_w(x)\nu x} f(x, \eta), \tag{9.1}$$

where only "+" sign has been considered in the transformation (6.5) which corresponds to the stretching sheet flow only. The case of shrinking wall velocities follows, however, in the similar way and has been discarded in this discussion. Because of Eqs. (6.5) and (9.1), the governing system (5.2)–(5.4) transforms to

$$\frac{x}{u_w}\frac{\mathrm{d}u_w}{\mathrm{d}x}\left(\frac{\partial f}{\partial \eta}\right)^2 - \frac{1}{2}\left(1 + \frac{x}{u_w}\frac{\mathrm{d}u_w}{\mathrm{d}x}\right) f\frac{\partial^2 f}{\partial \eta^2} + x\left(\frac{\partial f}{\partial \eta}\frac{\partial^2 f}{\partial \eta \partial x} - \frac{\partial^2 f}{\partial \eta^2}\frac{\partial f}{\partial x}\right) = \frac{\partial^3 f}{\partial \eta^3}, \tag{9.2}$$

$$\left.\begin{array}{ll} \frac{\partial f}{\partial \eta} = 1, f = 0, & \text{at } \eta = 0 \\ \frac{\partial f}{\partial \eta} = 0, & \text{at } \eta = \infty \end{array}\right\}. \tag{9.3}$$

In this case, the coefficient of skin-friction comes out of the form

$$\frac{1}{2}\sqrt{Re_x} C_f = \left.\frac{\partial^2 f}{\partial \eta^2}\right|_{\eta=0}; \; Re_x = \frac{u_w x}{\nu}. \tag{9.4}$$

It is worth noting here that the first two terms on the left-hand side of Eq. (9.2) own the variable coefficients involving $\frac{x}{u_w}\frac{\mathrm{d}u_w}{\mathrm{d}x}$ which is a function of x, in general. However, situations do exist, for example: $u_w(x) = ax^m$, when the coefficient $\frac{x}{u_w}\frac{\mathrm{d}u_w}{\mathrm{d}x}$ becomes a pure constant. In such situations, the last two terms, involving differentiation w.r.t. x on the left-hand side of Eq. (9.2), do not contribute any more. Consequently, the *pde* turns to an *ode*, thus representing the self-similar situation. Therefore, Eq. (9.2) can also be regarded as a generalization of the self-similar

Eq. (6.4) for the stretching sheet case which certainly reduces to Eq. (6.4) when the variable coefficients become constant. Particular to the case considered in this section, the non-similarity comes due to the wall velocity only. Equation (9.2) can further be recasted in a relatively simpler form, given by

$$2\frac{\xi}{u_w}\frac{\mathrm{d}u_w}{\mathrm{d}\xi}\left(\frac{\partial f}{\partial \eta}\right)^2 - f\frac{\partial^2 f}{\partial \eta^2} + 2\xi\left(\frac{\partial f}{\partial \eta}\frac{\partial^2 f}{\partial \eta \partial \xi} - \frac{\partial^2 f}{\partial \eta^2}\frac{\partial f}{\partial \xi}\right) = \frac{\partial^3 f}{\partial \eta^3}, \tag{9.5}$$

where the utilized change of variables reads as

$$\mathrm{d}\xi = \rho^2 \nu u_w(x)\mathrm{d}x, \quad \mathrm{d}\eta = \frac{\rho u_w(x)}{\sqrt{2\xi}}\mathrm{d}y, \quad \psi(x,y) = \sqrt{2\xi} f(\xi,\eta). \tag{9.6}$$

The coefficient of skin-friction and the momentum and displacement thicknesses in terms of the variables (9.6) take the form

$$C_f = \frac{\tau_w}{\frac{1}{2}\rho u_w^2} = \mu\sqrt{\frac{2}{\xi}}\frac{\partial^2 f}{\partial \eta^2}\bigg|_{\eta=0}, \tag{9.7}$$

$$\theta = \frac{\sqrt{2\xi}}{\rho u_w}\int_0^\infty u^2 \mathrm{d}\eta, \tag{9.8}$$

and

$$\delta^* = \frac{\sqrt{2\xi}}{\rho u_w}\int_0^\infty u\,\mathrm{d}\eta, \tag{9.9}$$

respectively.

9.2 Accelerated/Decelerated Non-similar Flows

All differentiable forms of $u_w(x)$, in addition to the power-law and exponential ones, are admissible by the system (9.2)–(9.3). However, the power-law and exponential wall velocities shall not be considered here because, with these forms of the wall velocity, system (9.2)–(9.3) reduces to the self-similar form, as mentioned earlier. Even with the exclusion of self-similar wall velocities, the family of non-similar wall velocities is still too large. It is therefore impossible to mention all such forms here and hence to analyze all of them. However, as an example, the Howarth's [1] (like) wall velocity of the form

$$u_w(x) = U_0 \pm ax, \tag{9.10}$$

is considered where U_0 denotes the constant wall velocity and a is a positive constant. The "+" sign refers to the accelerated wall velocity, while the "−" sign governs the retarded wall law.

Physically, the wall velocity (9.10) is a linear combination of the translating velocity and the linear stretching or shrinking velocity corresponding to the "+" or "−" sign, respectively. Thus, the shrinking sheet flow, being retarded in nature, is vulnerable to the separation phenomena, whereas the stretching sheet flow would involve no separation at all because of accelerated nature of it. With the selection of "−" sign in Eq. (9.10), it has been calculated that the coefficient of skin-friction decreases continuously till $x^*_{sep.} = 0.42$, where it becomes zero and changes its sign further onward to $x^*_{\text{sep.}}$. This fact has been depicted in Fig. 9.1 where the velocity graph tends to attain *S*-shape with increasing values of x^* till $x^*_{\text{sep.}} = 0.42$, where the velocity graph achieves the *S*-shape and the velocity curve shows the presence of point of inflection in it. The coefficient of wall skin-friction is shown plotted against x^* in Fig. 9.2 where the function $f''(x^*)$ can be seen hitting zero at $x^*_{\text{sep.}} = 0.42$. Due to Eqs. (9.6) and (9.10), the variables x^* and ξ are related as

$$\xi = \rho^2 \nu (1 \pm a x^*) x^*, \tag{9.11}$$

where $x^* = x/L$ with L denoting suitable characteristic length in the x-direction.

The numerical values of skin-friction coefficient listed in Table 9.1 correspond to different values of x^*. In comparison with the Howarth's retarded flow [1], the separation has been delayed by 250% in the present case. The reason behind this is the increased wall skin-friction in the moving continuous sheet flows as compared to the sheets of fixed length. Therefore, the increased wall friction thus assists the boundary-layer flow to survive a quite longer in the infinite continuous wall cases in comparison with the finite wall cases.

The stretching sheet case of the current non-similar flow involves no such trouble because of its accelerating nature. Upon advancing along the moving sheet in increasing x*-direction, the flow establishes more and more by confining itself to a narrower region near the moving continuous wall. The velocity graphs of this case

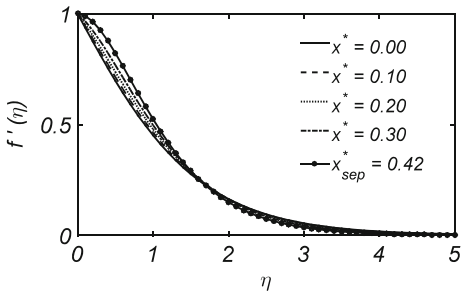

Fig. 9.1 Velocity graphs at different x* locations

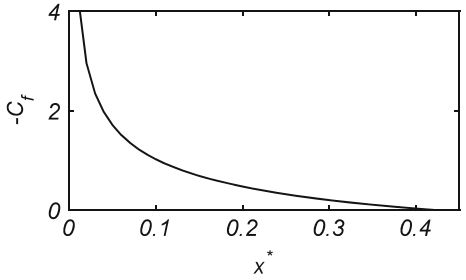

Fig. 9.2 Variation of coefficient of skin-friction while x^* approaches the separation point

Table 9.1 Dimensionless wall shear values

	$-\frac{\tau_w}{\rho U_0^2} Re_L^{1/2}$	
x^*	Shrinking case	Stretching case
0.01	4.3134	4.5644
0.05	1.7091	2.2704
0.1	1.0206	1.8139
0.15	0.6859	1.6566
0.2	0.4717	1.5912
0.25	0.3174	1.5670
0.3	0.1992	1.5653
0.35	0.1052	1.5771
0.38	0.0575	1.5886
0.40	0.0288	1.5977
0.42	0.0022	1.6078

are shown plotted in Fig. 9.3 where the velocity graphs can be seen decreasing upon increasing the values of x^*. Consequently, the coefficient of skin-friction increases as shown in Fig. 9.4 with x^*, thus avoiding the occurrence of flow separation. The numerical values of the coefficient of skin-friction have also been listed in Table 9.1 at different x^*-stations. The above-reported results have been obtained due to Eq. (9.5) subject to the boundary conditions (9.3).

For the two-dimensional and axially symmetric non-similar boundary-layer equations, the famous Keller-Box Method is the appropriate numerical tool which

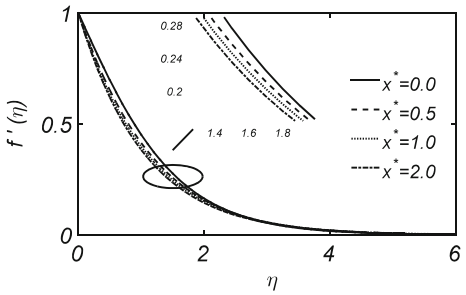

Fig. 9.3 Velocity profile for the accelerated case

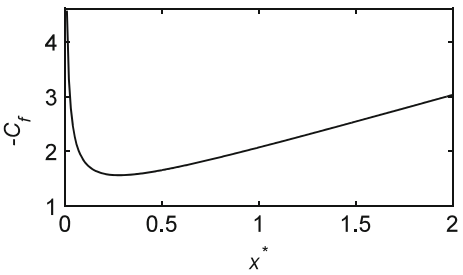

Fig. 9.4 Coefficient of skin-friction plotted against x^* (accelerated case)

Table 9.2 Accuracy of the method for Howarth's flow: dimensionless wall shear values

	$\frac{\tau_w}{\rho U_0^2} Re_L^{1/2}$	
x^*	Present method	Howarth's [1]
0.0125	2.742	2.739
0.0250	1.773	1.772
0.0375	1.310	1.309
0.0500	1.011	1.011
0.0625	0.790	0.790
0.0750	0.612	0.613
0.0875	0.458	0.459
0.1000	0.314	0.315
0.1125	0.163	0.163
0.1200	0.002	0.000

Table 9.3 Grid independence in ξ by fixing $\Delta\eta = 0.1$ and numerical infinity equal to 8.0

No. of points	$x^*_{\text{sep.}}$	$-\frac{\tau_w}{\rho U_0^2} Re_L^{1/2}$
15	0.42	0.0029
22	0.42	0.0026
43	0.42	0.0022
61	0.42	0.0022
85	0.42	0.0023
141	0.42	0.0023
422	0.421	0.0010

converges unconditionally. An introduction to this method has already been given in Sect. 4.2.2. The current solution has also been obtained because of this method. The accuracy of the utilized numerical procedure was first ensured by solving the famous Howarth's retarded flow. A comparison of the results obtained due to the current procedure with those of Howarth's [1] has been given in Table 9.2. Clearly, the current solution is in appreciable agreement with the Howarth's solution [1]. This authenticates our numerical procedure and allows for the integration of Eq. (9.5) with the aid of it. The grid independence check has also been applied to the current numerical procedure, and the results have been shown in Tables 9.3 and 9.4.

Table 9.4 Grid independence in η by taking numerical infinity equal to 8.0

	$\Delta\xi = 0.01$		$\Delta\xi = 0.001$	
No. of points	$x^*_{\text{sep.}}$	$-\frac{\tau_w}{\rho U_0^2} Re_L^{1/2}$	$x^*_{\text{sep.}}$	$-\frac{\tau_w}{\rho U_0^2} Re_L^{1/2}$
17	0.42	0.0016	0.421	0.0003
81	0.42	0.0022	0.421	0.0010
161	0.42	0.0024	0.421	0.0011
801	0.42	0.0024	0.421	0.0011

The data presented in these tables show that the current solution is independent of the grid for appropriate selection of the step sizes in ξ- and η-directions.

Normally, owing to the boundary-layer behavior, relatively big step sizes in ξ do produce the correct results, but regarding the capturing of separation point, the current analysis reveals that the dense grid provides the much better approximation in comparison with the coarse one. After several runs, the results reported in Table 9.1 were calculated by choosing $\Delta\xi = 0.01$ and $\Delta\eta = 0.1$ and taking (the numerical infinity) $\eta_\infty = 8.0$.

Reference

1. L. Howarth, On the solution of the laminar boundary layer equations. Proc. Roy. Soc. London A **164**, 547–579 (1938)